Chitosan-based scaffolds for tissue regeneration: Preparation and microstructure characterisation

ARTICLE · JANUARY 2016

READS
29

8 AUTHORS, INCLUDING:

Marco Vinícius Chaud
University of Sorocaba
85 PUBLICATIONS **434** CITATIONS
SEE PROFILE

Norberto Aranha
University of Sorocaba
33 PUBLICATIONS **253** CITATIONS
SEE PROFILE

Valquíria Miwa Hanai Yoshida
University of Sorocaba
17 PUBLICATIONS **7** CITATIONS
SEE PROFILE

José Martins de Oliveira Jr.
University of Sorocaba
59 PUBLICATIONS **277** CITATIONS
SEE PROFILE

EUROPEAN JOURNAL OF BIOMEDICAL AND PHARMACEUTICAL SCIENCES
http://www.ejbps.com

ISSN 2349-8870
Volume: 3
Issue: 1
15-24
Year: 2016

CHITOSAN-BASED SCAFFOLDS FOR TISSUE REGENERATION: PREPARATION AND MICROSTRUCTURE CHARACTERIZATION

Márcia A. Rebelo[1], Marco V. Chaud[1], Victor M. Balcão[1,2], Marta M. D. C. Vila[1], Norberto Aranha[1], Valquíria M. H. Yoshida[1], Thaís F. Alves[1] and José M. De Oliveira Jr[1*]

[1]LaFINAU / LaBNUS – Laboratory of Applied Nuclear Physics / Biomaterials and Nanotechnology Laboratory, i(bs)[2] – intelligent biosensing and biomolecule stabilization research group, University of Sorocaba, Sorocaba/SP, Brazil
[2]CEB - Centre of Biological Engineering, University of Minho, Braga, Portugal.

***Author for Correspondence: José M. De Oliveira Jr**
LaFINAU / LaBNUS – Laboratory of Applied Nuclear Physics / Biomaterials and Nanotechnology Laboratory, i(bs)[2] – intelligent biosensing and biomolecule stabilization research group, University of Sorocaba, Sorocaba/SP, Brazil.

Article Received on 03/11/2015 **Article Revised on 24/11/2015** **Article Accepted on 15/12/2015**

ABSTRACT
Scaffolds are porous three-dimensional supports, designed to mimic the extracellular environment and remain temporarily integrated into the host tissue while stimulating, at the molecular level, specific cellular responses to each type of body tissues. The major goal of the research work entertained herein was to study the microstructure of scaffolds made from chitosan (Ch), blends of chitosan and sodium alginate (Ch/NaAlg), blends of chitosan, sodium alginate and calcium chloride (Ch/NaAlg/$CaCl_2$) and blends of chitosan, sodium alginate and hydroxyapatite (Ch/NaAlg/HA). Scaffolds possessing ideal physicochemical properties facilitate cell proliferation and greatly increase the rate of recovery of a damaged organ tissue. Using µCT three-dimensional images of the scaffolds, it was observed that all scaffolds had a porosity in the range 64%-92%, a radius of maximum pore occurrence in the range 95µm-260µm and a permeability in the range 1×10^{-10}-18×10^{-10} m^2. From the results obtained, the scaffolds based on Ch, Ch/NaAlg and Ch/NaAlg/$CaCl_2$ would be most appropriate both for the growth of osteoid and for bone tissue regeneration, while the scaffold made with a blend of Ch/NaAlg/HA, by possessing larger pores size, might be used as a support for fibrovascular tissue.

KEYWORDS: tissue regeneration, chitosan scaffolds, computed tomography, porosity, permeability.

1. INTRODUCTION
Tissue engineering is an area that has experienced great advances in recent years, due to the ever increasing need to produce three-dimensional structures that can mimic and act as temporary Extracellular Matrices (ECM) for cell proliferation. The ECM, by being implanted in the place of damaged tissues should provide the mechanical support needed to ensure cell growth (Massai et al., 2014) which, added to a proper oxygenation and diffusion of nutrients (Hutmacher, 2000; Hollister, 2005; Spector, 2007; Tabata, 2009) will promote cell colonization, thus permitting the regeneration of damaged tissue. Many strategies have been proposed for obtaining such ECM, including the use of natural or synthetic materials (Wattanutchariya and Changkowchai, 2014; Murphy et al., 2000; Thomson et al., 1999; Peter et al., 1998; Murphy and Mooney, 1999). The choice of the ECM to be used depends on the type of tissue to be regenerated, the type and extent of damage which is intended to repair, the place of damage, among other parameters (Tabata, 2009). However, regardless of the type of ECM chosen, all should ensure proper mechanical and nutrient transport properties so as to ensure cell proliferation, which leads to an extensive list of materials and/or biomaterials that could be tested for tissue repair (Jones et al., 2004; Karageorgiou and Kaplan, 2005). The minimum physicochemical properties that a scaffold must present, to be used as support matrix for tissue regeneration, are biocompatibility (Chen et al., 2013), biodegradation (Tabata, 2009; Sultana and Wang, 2008), mechanical resistance (Leong et al., 2003), three-dimensional structure and adequate porosity (Mikos et al., 1993; Ranucci et al., 2000; Takahashi et al., 2005) with uniformly interconnected pores and of appropriate dimensions. The pore size of the scaffold must be compatible with the size of the cell phenotype of interest, and the porosity must be between 75% - 90% in order to promote cell attachment (Mikos et al., 1993; Ranucci et al., 2000). The diverse nature of the architectures of organic tissues requires pore dimensions in specific bandwiths compatible to each tissue. The ratio surface area / pore volume of the material depends on the average diameter and density of pores. However, the diameter of cells in suspension limits the minimum size of the pores, which vary from one cell type to another.

Depending on the intended application, the pore size should be carefully controlled. The effect of pore dimensions upon tissue regeneration is ensured by experimental studies that demonstrated an optimum porosity of 5 μm for neovascularization, 5-15 μm for fibroblast growth, near to 20 μm for hepatocyte growth, 20-125 μm for adult mammalian skin regeneration, 40-100 μm for osteoid growth, and 100-350 μm for bone regeneration (Klawitter and Hulbert, 1971; Wake et al., 1994; Wang et al., 1999). Fibrovascular tissue requires pores larger than 500 μm for a rapid vascularization and survival of transplanted cells (Yang et al., 2001). In the research effort entertained herein, a novel and somewhat pioneering approach is proposed for the topological and morphological characterization of scaffolds made of chitosan (Ch), blends of chitosan and sodium alginate (Ch/NaAlg), blends of chitosan, sodium alginate and calcium chloride (Ch/NaAlg/$CaCl_2$), and blends of chitosan, sodium alginate and hydroxyapatite (Ch/NaAlg/HA). Physical properties of these scaffolds, such as porosity, pore size distribution, spatial correlation and (inter)connectivity of the porous matrix, permeability, among others, were assessed using two- and three-dimensional images of the scaffolds, gathered via computed microtomography by high-resolution X-ray transmission.

2. MATERIALS AND METHODS

2.1. Materials

2.1.1. Chemicals. All reagents used were of analytical grade or better, and were used without further purification. Tap water was purified in a Milli-Q Elga Purelab system (Molsheim, France) to a final conductivity of ca. 18.2 $M\Omega.cm^{-1}$. Chitosan (200-800 cP), sodium alginate (4-12 cP), and hydroxyapatite ($Ca_3(PO_4)_2$, purity ≥ 90%) were all purchased from Sigma-Aldrich (St. Louis MO, USA).

2.1.2. Analytical equipment. A computed tomographer via X-ray transmission from Bruker microCT (model SkyScan 1174, Kontich, Belgium) was utilized in all non-destructive analyses, for gathering tomographic images of the chitosan-based scaffolds. The analysis software utilized for processing the tomographic images were CTVox™ (version 2.6.0 r908-64bit, from Bruker microCT) and CTan™ (version 1.13.5.1-64bit, from Bruker microCT) and CTvol (version 2.2.3.0-64bit, from Bruker microCT). For the analyses of pore size distribution, calculation of the correlation functions and pore connectivity and determination of permeability, the software IMAGO® (Image Analysis System, version 2.4.11) was duly utilized.

2.2. Experimental procedures

2.2.1. Preparation of chitosan-based scaffolds. Chitosan matrices were prepared using chitosan (viscosity between 200-800 cP), sodium alginate (viscosity between 4-12 cP) and hydroxyapatite ($Ca_{10}(PO_4)_6(OH)_2$, with a purity higher than 90%). The scaffolds of chitosan (Ch) and of blends of chitosan with sodium alginate (NaAlg) were prepared via lyophilization of aqueous dispersions of Ch and Ch/NaAlg. Aqueous dispersions of Ch and of NaAlg were prepared under mechanical stirring (at ca. 7200 rpm during 10 min) using an UltraTurrax (model T25D from IKA Werke GmbH & Co. KG, Staufen, Germany) homogenizer equipped with a 25G dispersing element at a constant temperature (ca 25 °C). The aqueous dispersion of Ch/NaAlg blends was obtained by mixing the aqueous formulations of Ch and NaAlg at a ratio of 1:1 (w/w). The mixtures thus produced were homogenized using a 25G dispersing element under the same aforementioned conditions. To prepare the scaffolds, ca. 3 g of each aqueous formulation of Ch and Ch/NaAlg were poured into a cylindrical mold with volumetric capacity of 7 cm^3, frozen to -80 ºC (in a Ultra-freezer from Cold Lab, Piracicaba, Brazil) and lyophilized (in a lyophilizer from Thermo Fisher Scientific, model D115, Massachusetts, USA). Subsequently, the scaffold obtained from formulation of the blend Ch/NaAlg was submerged in a solution of $CaCl_2$ 200 $mmol.dm^{-3}$ during 10 min and successively washed with ultrapure water until reaching a pH of 6.2. The scaffolds treated with $CaCl_2$ received the designation of Ch/NaAlg/$CaCl_2$. Water elimination was carried out by evaporation at room temperature (ca. 25 °C ± 1 ºC) until reaching constant weight. The scaffold samples were stored at room temperature and in the dark. To prepare the scaffolds with hydroxyapatite (HA), one selected the Ch/NaAlg blends. HA was incorporated in the formulation at the mass ratios (Ch:NaAlg:HA) of 1:1:0.2; 1:1:0.4 and 1:1:0.6 (w/w). HA was standardized in a sieve (with a mesh 60) and slowly added to the aqueous dispersion of NaAlg under mechanical stirring (at ca. 7200 rpm during 10min). The chitosan dispersion was added to the NaAlg/HA blend under the same conditions until complete homogenization. To prepare the scaffolds, ca. 3g of each formulation were poured into a cylindrical mold with volumetric capacity of 7 cm^3, frozen at -80 ºC and duly lyophilized.

2.2.2. Tomographic imaging. The tomographic images were gathered placing the scaffold samples in the interior of the tomograph chamber. Image slices were obtained using the following configurations of the tomographic system: operating voltage set at 35 kV and electric current with 800 μA. The technique employed for obtaining a tomographic image involved the acquisition of a large number of radiographs of the object (image slices), obtained by measuring the intensity of X-rays transmitted through the sample, at different angular positions. The scaffold samples of Ch, Ch/NaAlg, Ch/NaAlg/$CaCl_2$ and Ch/NaAlg/HA were rotated by 180 degrees, with an angular step of 1 degree, thus producing 180 radiographs (projections) per image, each containing 652×652 pixels with a spatial resolution of 24 μm for Ch and of 28.7 μm for the other scaffold samples. At the outlet of the X-ray source one utilized a filter of Al with 0.25 mm thickness. Appropriate mathematical algorithms were then used to reconstruct the three-dimensional

tomographic image (3D) of the scaffold samples, through appropriate composition of bi-dimensional images (2D). The three-dimensional images possessed 652×652×652 pixels and the same spatial resolution of the 2D images, and thus the volume of data generated for each scaffold sample was isotropic with relation to the spatial resolution. Having gathered all the projections (radiographs gathered at each angular position), one utilized the software NRecon™ from Bruker (version 1.6.9.4, Kontich, Belgium), which uses the algorithm of Feldkamp *et al*. (1984) in the process of reconstruction of the tomographic images.

2.2.3. Theoretical calculations. Following a mathematical treatment, the bidimensional images (2D) were used to generate the three-dimensional images (3D) either via direct rendering of volume (Lacroute, 1995; Oliveira Jr. et al., 2005) or using mathematical models (Bouvier, 2000). The segmentation of images and binarization (Gonzales and Woods, 1992) consists in the separation of the regions of interest and subsequent creation of images in black and white tones. The Double-Time Cubes algorithm (Bouvier, 2000) (a fast 3D surface construction algorithm for volume visualization) was used to produce the 3D images, based in a mathematical model. Following segmentation and binarization, the 2D or 3D tomographic images can then be used to characterize a material. The porosity and permeability are the properties most usually used in the characterization of a porous material. Porosity refers to the volume that can be occupied by a fluid in a porous structure, and permeability refers to the ability of the porous structure to allow the flow of the stored fluid. In the same way, when one wants to characterize the porous microstructure departing from planar sections (2D images) of the material, geometric parameters are measured, such as the correlation function or the connectivity, the pore size distribution, or the distribution of linear ropes. According to Pennella *et al*. (2013), the internal microstructure of a porous matrix can be characterized dividing the porous medium into a discrete and well defined collection of individual pores. Hence, the pore may be defined as an empty region of space surrounded by solid surfaces. Within this context, porosity φ is defined as Equation (1):

$$\varphi = \frac{V_V}{V_T} \quad (1)$$

where V_V is the volume of porous space and V_T is the total volume of the material. From the point of view of tissue growth, besides porosity, characterization of the scaffolds by using statistical functions such as pore size distribution has been important. The study of the size distribution of objects is commonly called granulometry (Coster and Chermant, 1989). To determine the pore size distribution, several morphological openings are used (Coster and Chermant, 1989) with a sequence of structuring elements of increasing size, δ_1, δ_2, … δ_{max}, where δ_{max} is such that it eliminates all pores in the operation of erosion. For the determination of pore distribution in 2D images, the unit of measure consists in the surface area of the pores. In this way, the cumulative distribution of pores is given by Equation (2).

$$F(r) = \frac{\varphi - \varphi(r)}{\varphi} \quad (2)$$

where $F(r)$ is the fraction of pore sizes equal or smaller than r, φ is the total porosity of the departing image, and $\varphi(r)$ is the image porosity following opening with a disk of radius r. The starting porosity, φ, is produced from the ratio between the pixels belonging to the porous phase and the total pixels of the image. Porosity $\varphi(r)$ is obtained via the same procedure, but after repeated openings, increasing the value of r, until all porosity is eliminated by this operation. Within the context of statistical processing of the images, a digital image may be considered as a matrix, meaning that it can be considered as a stochastic process (process of random nature) (Fernandes et al., 1996; Fernandes, 1994). This greatly enhances the easiness in the analysis of image characteristics. In a binary image, one can define the so-called phase functions, $\Im$, associated with the two phases (phase 1 = matter; phase 2 = pore) of the image components, as follows (Equation (3)).

$$Z_{\Im}(r) = \begin{cases} 1, \text{ if } r \text{ belongs to phase } \Im \\ 0, \text{ if not} \end{cases} \quad (3)$$

where r denotes a position vector relative to an arbitrary origin, and $\Im$ can be phase 1 or phase 2. The mathematics of stochastic processes allows us to observe their characteristics. These characteristics are called moments. They represent the probability to achieve a desired result. For example, in an image, one chooses any one pixel and the chance that this pixel belongs to a pore is observed, thus producing a first order moment. By observing the chance that two any pixels, separated by a certain distance r, belong to a pore, a moment of second order is produced, and so on. The first order moment is defined as Equation (4).

$$\varphi_{\Im} = < Z_{\Im}(r) > \quad (4)$$

where symbol < > denotes the statistical average for the image domain under consideration. For images of porous substances, the first order moment is nothing more than a measure of porosity. With the hypothesis of a statistically homogeneous medium, we define the correlation function or autocorrelation for each $\Im$ phase, for every arbitrary shift u, as Equation (5).

$$C_{\Im}(u) = < Z_{\Im}(r) \cdot Z_{\Im}(r+u) > \quad (5)$$

The autocorrelation function gives the probability that two pixels separated by a distance u belong to the phase under consideration. The $\varphi_{\Im}$ porosity and the autocorrelation function $C_{\Im}(u)$ correspond to the first two moments of the phase function $Z_{\Im}(r)$. For a 2D binary image, one can define another function called connectivity, as being the probability that a rope (a line segment with the end at the phase interfaces) randomly chosen at the pore phase or matter phase, with a certain length u, belongs to the phase object of study (Torquato, 1993). The procedure consists in launching a large number of ropes with sizes larger than the dimensions of the image, and count the number of rope sections that are totally located in the interior of the chosen phase $\Im$ and, furthermore, belong to the same connected component of phase $\Im$. Thus, the connectivity function can be defined as (Fernandes et al., 1996) Equation (6).

$$P_{\Im}(r) = \begin{cases} k, \text{ if } r \text{ belongs to component } k \text{ of phase } \Im \\ 0, \text{ if not} \end{cases} \quad (6)$$

Another property commonly used in the characterization of porous space is the permeability. Permeability is the property that refers to the measure of the ability of a porous medium to allow fluid flow. When only one fluid entirely fills the porous space, one gets the absolute or intrinsic permeability, which depends entirely and solely on the porous space configuration. According to Darcy's model, considering unidirectional flow at low speed, in a sample of length l and cross-sectional area A, subjected to a pressure difference ΔP, one can calculate the flow rate Q as Equation (7).

$$Q = \frac{k \cdot A}{\mu} \times \left(\frac{\Delta P}{l} \right) \quad (7)$$

where k is the absolute permeability of the medium and μ is the fluid viscosity. In the International System of Units, permeability is expressed in m^2, but usually the unit used is the Darcy (D), with 1D = 0.987×10^{-12} m^2. In the present research effort, the permeability was determined by the *Fast k* method (Damiani et al., 2000) using the software IMAGO® (Imago® User Manual, 2002). To determine the permeability via this method, one assumes a cubic domain, where the structure of the material is represented as the superposition of several mono-scale percolation networks, where in each network the elements that represent the pores and the solids are arranged in a random fashion. The input data are the pore size distribution and the solid size distribution. Assuming a Poiseuille flow, the permeability as calculated by the *Fast k* method, for a pore of class i with diameter d_i is calculated as Equation (8).

$$k_i = \frac{d_i^2}{28.4} \quad (8)$$

with the pore size distribution obtained from 2D images.

3. RESULTS AND DISCUSSION

The microstructure of porous materials, such as those presented by chitosan scaffolds, have complex geometries involving both the form and the distribution and connectivity of pores. The chemical composition of these scaffolds plays an important role, since they are related to the properties of biocompatibility and biodegradability of the biomaterial which, added to the physical characteristics, will indicate whether the scaffold porous matrix meets the minimum requirements needed for cell colonization. Ideally, all physical and chemical tests should be performed on the scaffold itself that is intended to be implanted. For this to be possible, non-destructive tests should be carried out. Within this context, the physical analyzes performed to the chitosan scaffolds under study are presented next. Figure 1 displays the three-dimensional tomographic images of the several scaffolds, obtained by direct volume rendering, being **(a)** Ch scaffold, **(b)** Ch/NaAlg scaffold, **(c)** Ch/NaAlg/$CaCl_2$ scaffold and **(d)** Ch/NaAlg/HA scaffold.

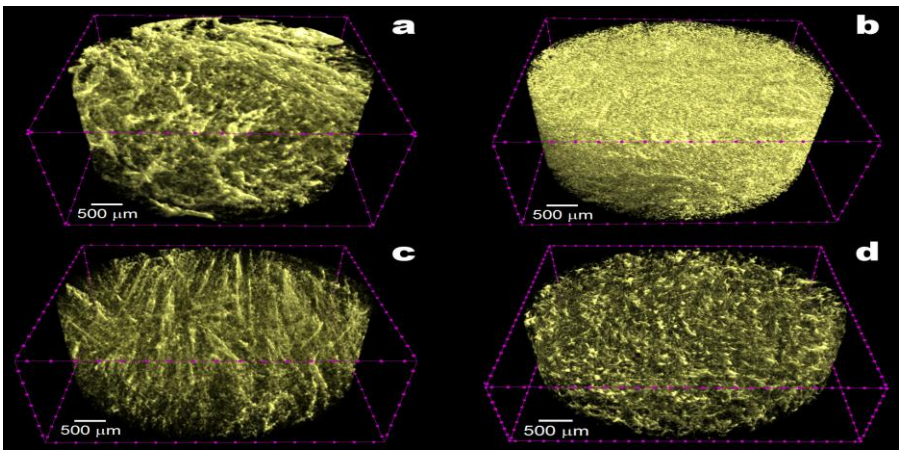

Figure 1: Reconstructed three-dimensional tomographic images of the scaffolds using direct volume rendering, for (a) Ch scaffold, (b) Ch/NaAlg scaffold, (c) Ch/NaAlg/$CaCl_2$ scaffold and (d) Ch/NaAlg/HA scaffold.

The three-dimensional structures of the scaffolds shown in Figure 1 present different morphological characteristics, whose quantification was done by measuring the porosity, pore size distribution, the spatial correlation function and connectivity of the pores, the permeability of the porous structure, among other parameters. Table 1 displays the main geometric parameters quantified in the present research effort.

Table1. Geometric parameters of the chitosan-based scaffolds prepared.

Scaffold type	Total porosity (%)	Permeability ($\times 10^{-10}$ m^2)	Closed porosity (%)	Radius (μm)/ percentage of maximum occurrence of pores (%)	Connectivity density of material/pores ($\times 10^7$ mm^{-3})
Ch	64.0 ± 2.5	1.12 ± 0.15	0.36	95 (24)	9.3 / 9.4
Ch/NaAlg	75.0 ± 0.5	1.50 ± 0.04	0.23	85 (45)	24.4 / 8.9
Ch/NaAlg/$CaCl_2$	77.6 ± 0.6	2.00 ± 0.12	0.25	100 (30)	9.1 / 4.5
Ch/NaAlg/Hap	91.8 ± 0.3	18.20 ± 0.92	0.17	260 (13)	1.3 / 0.4

The scaffolds showed distinct physical properties, with porosity values ranging between a minimum of 64% and a maximum of 92%. An important feature exhibited by all the scaffolds examined in the present study is the small presence of closed pores (< 0.36%), which increases both the permeability and connectivity, ensuring that the transport of nutrients into the core of the scaffold is maximized. One way to visualize how the pores are distributed within the structure of the scaffolds is by reconstructing the three-dimensional scaffold structure (both pores and matter), using mathematical models. Figure 2 displays the three-dimensional tomographic images of the scaffolds, reconstructed using the mathematical algorithm Double-Time Cubes (25), being: **(a)** Ch scaffold (Vol = 26 mm^3), **(b)** Ch/NaAlg scaffold (Vol = 30 mm^3), **(c)** Ch/NaAlg/$CaCl_2$ scaffold (Vol = 30 mm^3) and **(d)** Ch/NaAlg/HA scaffold (Vol = 32 mm^3), with the dark color (brown) representing the solid phase and the light color (gray) representing the porous phase of the scaffold. All the images were reconstructed using a volume of approximately 30 mm^3, which is about the minimum volume representative of the object. From the visual analysis of the images shown in Figure 2, it can be observed that all have a high porosity with connected pores, with image **(b)** visually exhibiting pores with smaller diameters than the rest of the scaffolds, and image **(d)** visually exhibiting pores with larger diameters.

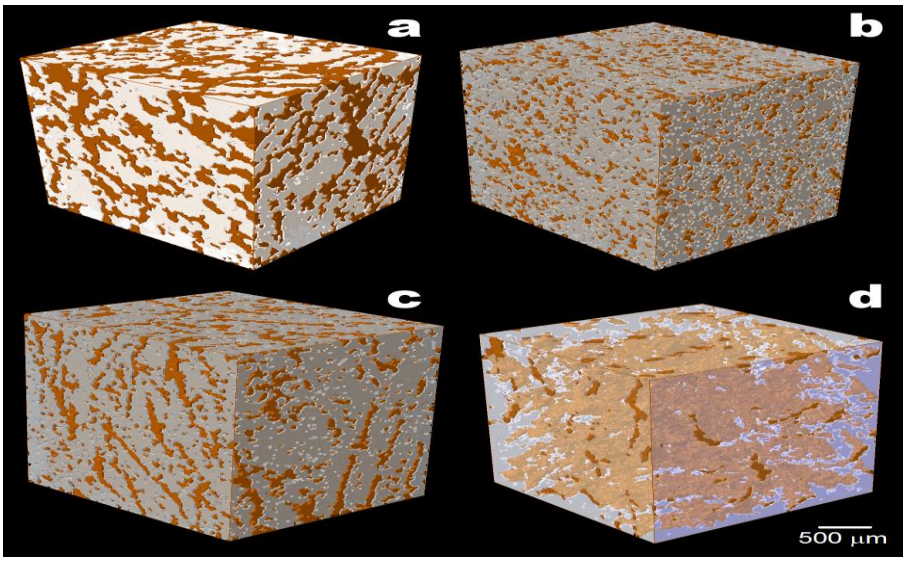

Figure 2: Reconstructed three-dimensional tomographic images of the scaffolds using the mathematical algorithm Double-Time Cubes, for (a) Ch scaffold (Vol = 26 mm^3), (b) Ch/NaAlg scaffold (Vol = 30 mm^3), (c) Ch/NaAlg/$CaCl_2$ scaffold (Vol = 30 mm^3) and (d) Ch/NaAlg/HA scaffold (Vol = 32 mm^3), with the dark color (brown) representing the solid phase and the light color (gray) representing the porous phase.

As a way of quantifying the physical properties of the scaffolds, Figure 3 displays the connectivity function for the several scaffolds, which provides the probability that two pixels separated by a distance *u* belong to the porous matrix and be in the core of the same pore, i.e. are connected. In Figure 3, curves **(a)**, **(b)**, **(c)** and **(d)** show that pixels belonging to the porous phase, whose separation is approximately lower than 200 μm, 150 μm, 250 μm and 350 μm, respectively, show an increase in the spatial correlation and connectivity, thus indicating the expected average diameter for the pores.

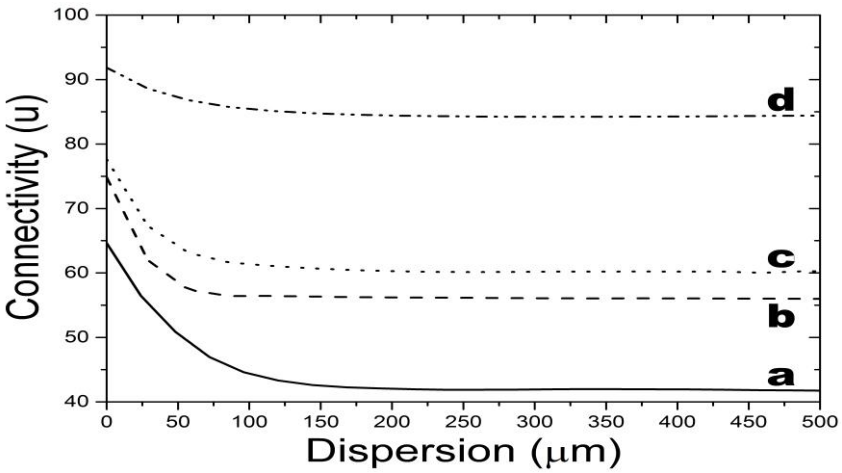

Figure 3: Connectivity as a function of the separation distance, *u* (dispersion), of the pixels, for (a) Ch scaffold, (b) Ch/NaAlg scaffold, (c) Ch/NaAlg/$CaCl_2$ scaffold and (d) Ch/NaAlg/HA scaffold.

The fact that two pixels belong to the same phase, i.e. being correlated, does not guarantee that they are in the core of the same pore, i.e. are connected. For all scaffolds analyzed in this work, the functions spatial correlation and connectivity showed a great similarity, indicating that the porous space is highly correlated, that the pores are connected and that the percentage of closed pores is small, thus favoring the transport of nutrients into the core of the scaffolds. Another important factor used in the characterization of a porous structure is the pore size distribution. Figure 4 displays the pore size distributions for the scaffolds utilized in the present research effort: **(a)** Ch, **(b)** Ch/NaAlg, **(c)** Ch/NaAlg/$CaCl_2$ and **(d)** Ch/NaAlg/HA. By analyzing the distributions in Figure 4, one notices that the maximum frequency of pores for the scaffolds Ch, Ch/NaAlg, Ch/NaAlg/$CaCl_2$ and Ch/NaAlg/HA, occurs for pores with radii around 95 μm, 85 μm, 100 μm and 260 μm, with a frequency of 24%, 45%, 30%, and 13%, respectively. The scaffold of Ch/NaAlg was the one that presented the highest frequency of pores with smaller radii, while the scaffold Ch/NaAlg/HA was the one that presented the highest occurrence of pores with larger radii. The scaffold of Ch/NaAlg has more than 40% of the pores centered around 85 μm and another 45% not differing more than 30% of the central value. This shows that the scaffold Ch/NaAlg exhibits a high uniformity in pore size distribution.

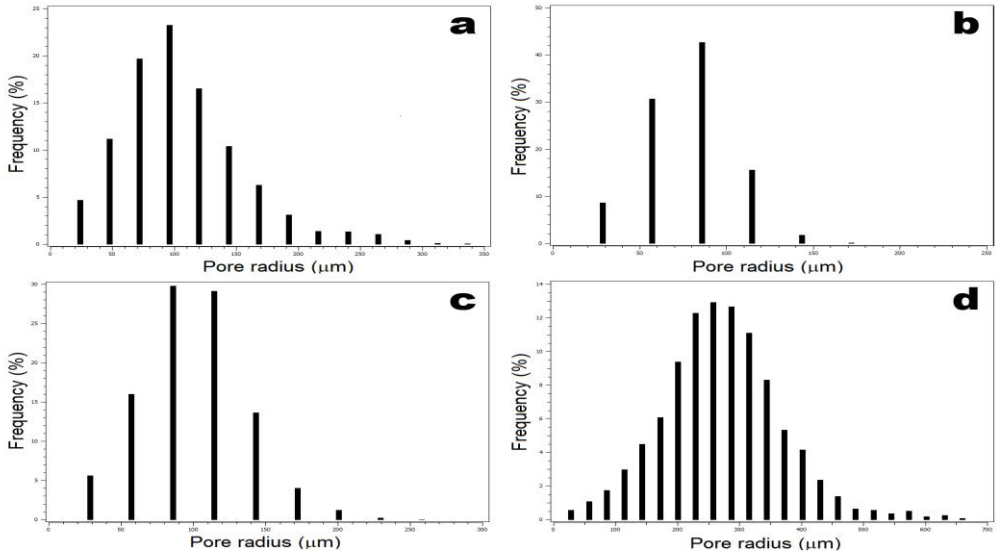

Figure 4: Pore size distribution for (a) Ch scaffold, (b) Ch/NaAlg scaffold, (c) Ch/NaAlg/$CaCl_2$ scaffold and (d) Ch/NaAlg/HA scaffold.

The pore distribution of the scaffold Ch/NaAlg/$CaCl_2$ presents approximately 60% of the pores with a radius of 100 μm and pores with a maximum radius around 250 μm. The scaffold of Ch/NaAlg/HA was the one that presented the most significant differences compared to the others, since beside having larger pores, with pore size distribution centered around the radius of 260 μm, its pores extended up to a radius of 650 μm, exhibiting a porous structure quite different from the other scaffolds. The knowledge of pore size distribution and their density in the ECM is important, since these factors directly influence the tissue growth. To be able to grow in an

ECM, each tissue requires a specific pore size distribution, depending on the diameter of the cells in suspension that are desired to grow in the ECM. The data obtained in the research work entertained herein, pertaining to pore size distribution, indicates that the scaffolds of Ch, Ch/NaAlg and Ch/NaAlg/$CaCl_2$ would be appropriate for the growth of osteoid (the unmineralized, organic portion of the bone matrix that forms prior to maturation of bone tissue) and bone tissue regeneration, since for growing these tissues require pores with radii of the order of 20 µm up to 175 µm. The scaffold made of Ch/NaAlg/HA, by having larger pores, might be used as support for growth of fibrovascular tissue, since for growing and for a rapid vascularization with concomitant survival of transplanted cells, this tissue requires pores with radii of the order of 250 µm. Another important factor for the success of tissue growth is the uniformity of the ECM. From the data displayed in Table 1, one can see that the scaffolds produced have a high density of connections, both in the porous phase and in the solid phase, indicating a great uniformity in the ECM. Finally, to ensure that an ECM succeeds, with respect to tissue growth, the amount of closed pores must be small so as to permit an adequate fluid flow within the ECM. One way to quantify such fluid flow is by measuring the permeability of the ECM. Table 1 shows that all the scaffolds used in this study presented a closed porosity smaller than 0.36% and a permeability ranging from approximately 1×10^{-10} m^2 to 18×10^{-10} m^2, wherein the scaffold with higher permeability was Ch/NaAlg/HA, since this scaffold presents the highest total porosity, the smallest closed porosity, and pores with larger dimensions and highly correlated and connected. The data in Table 2 provides a comparison of the scaffold porosity and permeability obtained in this study, with results published in the specialty literature. No data was found in the literature concerning measures of the permeability of scaffold structures made of chitosan, comparable to those of the present study. When comparing the values of permeability produced in the present research effort (1×10^{-10}-18×10^{-10} m^2) with the data gathered in the specialty literature for similar systems used for tissue regeneration, a clear agreement was found.

Table 2. Comparison of the data obtained in the present research effort with values reported in the specialty literature.

Scaffold system	Porosity (%)	Permeability ($\times10^{-10}$ m^2)	Reference
Ch	64.0 ± 2.5	1.12 ± 0.15	This work
Ch/NaAlg	75.0 ± 0.5	1.50 ± 0.04	This work
Ch/NaAlg/CaCl2	77.6 ± 0.6	2.00 ± 0.12	This work
Ch/NaAlg/Hap	91.8 ± 0.3	18.20 ± 0.92	This work
Ti alloy (Ti6Al4V)	56.7	0.52 ± 0.04	Truscello *et al*., 2012
PLLA	72.9	2.43 ± 0.15	Acosta Santamaría *et al*., 2012
Wax	30 - 70	1.5 - 15	Dias *et al*., 2012
45S5 Bioglass® -based	90 - 95	19.6 ± 1.1	Ochoa *et al*., 2009
Hydroxyapatite	72 - 80	4 - 32.4	Innocentini *et al*., 2009
PPF	50 - 64	15 - 23	Lee *et al*., 2006
BCP Dytech	80	1	Li *et al*., 2003
Hydroxyapatite	72 - 90	0.122 - 4.31	Sepulveda *et al*., 2001
Human–proximal femur (longitudinal)	-----	27.6	Lim and Hong, 2000
Human–proximal femur (transverse)	-----	1.2	Lim and Hong, 2000
Human–calcaneal	78 - 92	4 - 110	Grimm and Williams, 1997
Human–proximal tibia	-----	76.8	Beaudoin *et al*., 1991

By comparing the permeability data produced in the present study with values obtained for the permeability of human bone tissue, we observe that the values have the same order of magnitude, supporting the conclusion obtained from the analysis of pore size distribution. Finally, comparing the average permeability values produced in this study to those encountered in the literature, due to similarity, one may conclude that the method used to obtain the scaffold permeability (Fast *k* method) provides results within the range of expected values.

4. CONCLUSIONS

Chitosan-based scaffolds were produced using four distinct formulations. For each scaffold, two- and three-dimensional tomographic images were obtained. Direct volume rendering techniques were used (Lacroute, 1995; Oliveira Jr. et al., 2005) together with the mathematical algorithm Double-Time Cubes (Bouvier, 2000), to obtain the tomographic images in 3D, departing from 2D images. The analysis of tomographic images (2D or 3D) provided the physical parameters used in the topological and morphological characterization of the scaffolds, being the main parameters obtained porosity, connectivity function, pore size distribution and permeability. When analyzed together, all these parameters allowed the morphological and topological characterization of the scaffolds. It was possible to determine for which types of tissue growth each of the scaffolds would be more appropriate. The values produced for the porosity, added to the information of pore size distribution and to the permeability data, indicate that the scaffolds Ch, Ch/NaAlg, and Ch/NaAlg/$CaCl_2$ would be appropriate for the growth of osteoid and regeneration of bone tissue, whereas the scaffold Ch/NaAlg/HA (although presenting larger pores) could be used as support for the growth of both bone tissue and fibrovascular tissue. The values produced for the porosity (60-92%) and permeability (1×10^{-10}-18×10^{-10} m^2) are within the range of values reported in the literature. No data was found in the literature for scaffolds similar to those produced and used in the present study, to serve as a benchmark for permeability data. When comparing the scaffold permeability data obtained in this study with published data for other systems and for human bone tissue, it was found that the permeability of the scaffolds obtained by the Fast *k* method has the same order of magnitude. It has been shown, in the present research effort, that it is possible to perform a complete microstructural characterization of a scaffold, departing only from high resolution tomographic images of the scaffold.

5. ACKNOWLEDGEMENTS

Project funding by Fundação de Amparo à Pesquisa do Estado de São Paulo (FAPESP, São Paulo, Brazil) (**FAPESP Refs. No. 2012/21219-5, 2012/15651-4, 2013/03181-6, 2013/19300-4, and 2014/21122-0**), is hereby gratefully acknowledged. This work received support from CNPq, National Council for Scientific and Technological Development – Brazil, in the form of Research Productivity (PQ) fellowships granted to Victor M. Balcão and Marco V. Chaud. The authors have no conflicts of interest whatsoever to declare.

6. REFERENCES

1. Massai, D.; Pennella, F.; Gentile, P.; Gallo, D.; Ciardelli, G.; Bignardi, C.; Audenino, A.; Morbiducci, U. Image-Based Three-Dimensional Analysis to Characterize the Texture of Porous Scaffolds. BioMed Research International, 2014, 2014, Article ID 161437, 8 pages, 2014. doi:10.1155/2014/161437.
2. Hutmacher, D. W. Scaffolds in tissue engineering bone and cartilage. Biomaterials, 2000; 21: 2529–2543.
3. Hollister, S. J. Porous scaffold design for tissue engineering. Nature Materials, 2005; 4: 518–524.
4. Spector, M. Biomaterials-based tissue engineering and regenerative medicine solutions to musculoskeletal problems. Swiss Med. Wkly. 2007; 137: 157S-165S.
5. Tabata, Y. Biomaterial technology for tissue engineering applications. Journal of the Royal Society Interface, 2009; 6: S311-S324.
6. Wattanutchariya, W.; Changkowchai, W. Characterization of Porous Scaffold from Chitosan-Gelatin/Hydroxyapatite for Bone Grafting. Proceedings of the International MultiConference of Engineers and Computer Scientists, 2014, Vol. II, IMECS 2014, March 12 - 14, 2014, Hong Kong.
7. Murphy, W. L.; Kohn, D. H.; Mooney, D. J. Growth of continuous bonelike mineral within porous poly (lactide-co-glycolide) scaffolds in vitro. J. Biomed. Mater. Res. 2000; 50: 50-58.
8. Thomson, R. C.; Mikos, A. G.; Beahm, E.; Lemon, J. C.; Satterfield, W. C.; Aufdemorte, T. B.; Miller, M. J. Guided tissue fabrication from periosteum using preformed biodegradable polymer scaffolds. Biomaterials, 1999; 20: 2007-2018.
9. Peter, S. J.; Miller, M. J.; Yasko, A. W.; Yaszemski, M. J.; Mikos, A. G. Polymer concepts in tissue engineering. J. Biomed. Mater. Res. 1998; 43: 422-427.
10. Murphy, W. L.; Mooney, D. J. Controlled delivery of inductive proteins, plasmid DNA and cells from tissue engineering matrices. J. Periodontal Res. 1999; 34: 413-419.
11. Jones, A. C.; Milthorpe, B.; Averdunk, H.; Limaye, A.; Senden, T. J.; Sakellariou, A.; Sheppard, A. P.; Sok, R. M.; Knackstedt, M. A.; Brandwood, A.; Rohner, D.; Hutmacher, D. W. Analysis of 3D bone ingrowth into polymer scaffolds via micro-computed tomography imaging. Biomaterials, 2004; 25: 4947-4954.
12. Karageorgiou, V.; Kaplan, D. Porosity of 3D biomaterial scaffolds and osteogenesis. Biomaterials, 2005; 26: 5474-5491.

13. Chen, Q.; Lianga, S.; Thouasb, G. A. Elastomeric biomaterials for tissue engineering. Progress in Polymer Science, 2013; 38: 584-671.
14. Sultana, N.; Wang, M. Fabrication of HA/PHBV composite scaffolds through the emulsion freezing/freeze-drying process and characterisation of the scaffolds. J. Mater. Sci. Mater. Med. 2008; 19: 2555-2561.
15. Leong, K. F.; Cheah, C. M.; Chua, C. K. Solid freeform fabrication of three-dimensional scaffolds for engineering replacement tissues and organs. Biomaterials, 2003; 24: 2363-2378.
16. Mikos, A. G.; Sarakinos, G.; Lyman, M. D.; Ingber, D. E.; Vacanti, J. P.; Langer, R. Prevascularization of porous biodegradable polymers. Biotechnology and Bioengineering, 1993; 42: 716-723.
17. Ranucci, C. S.; Kumar A.; Batra, S. P.; Moghe, P. V. Control of hepatocyte function on collagen foams: sizing matrix pores toward selective induction of 2-D and 3-D cellular morphogenesis. Biomaterials, 2000; 21: 783-793.
18. Takahashi, Y.; Yamamoto, M.; Tabata, Y. Osteogenic differentiation of mesenchymal stem cells in biodegradable sponges composed of gelatin and beta-tricalcium phosphate. Biomaterials, 2005; 26: 3587-3596.
19. Klawitter, J. J.; Hulbert, S. F. Application of porous ceramics for the attachment of load-bearing internal orthopedic applications. J. Biomed. Mater. Res. Symp. 1971; 5: 161-229.
20. Wake, M. C.; Patrick, C. W.; Mikos, A. G. Pore morphology effects in the fibrovascular tissue growth in porous polymer substrates. Cell Transplant. 1994; 3: 339-343.
21. Whang, K.; Healy, E.; Elenz, D. R.; Nam, E. K; Tsai D. C.; Thomas C. H.; Nuber G. W.; Glorieux F. H.; Travers R.; Sprague S. M. Engineering bone regeneration with bioabsorbable scaffolds with novel microarchitecture. Tissue Eng. 1999; 5: 35-51.
22. Yang, S.; Leong, K. F.; Du, Z.; Chua, C. K. The Design of Scaffolds for Use in Tissue Engineering. Part I. Traditional Factors, Tissue Engineering, 2001; 7: 679-689.
23. Lacroute, P. G. Fast volume rendering using a shear-warp factorization of the viewing transformation, Technical Report: CSL-TR-95-678, 1995.
24. Oliveira Jr, J. M.; Lima, F. Z. C.; Milito, J. A.; Martins, A. C. G. Development and Applications of Three-dimensional Gamma Ray Tomography System Using Ray Casting Volume Rendering Techniques, Brazilian Journal of Physics, 2005; 35: 789-792.
25. Bouvier, D. J. Double Times Cubes: a fast surfacee construction algorithm for volume visualization. Unpublished report, University of Arkansas, 313 Enginneering Hall, Fayetteville, AR 72701, USA, 2000.
26. Gonzales, R. C.; Woods, R. E. Digital Image Processing. Addison-Wesley Publishing Company, 1992.
27. Pennella, F.; Cerino, G.; Massai, D.; Gallo, D.; Falvo D'Urso, L. G.; Schiavi, A.; Deriu, M. A.; Audenino, A.; Morbiducci, U. A survey of methods for the avaluation of tissue enginneering scaffold permeability. Annals of Biomedical Enginneering, 2013; 41: 2017-2041.
28. Coster, M.; Chermant, J.-L. Precis D'analyse D'images. Presses du CNRS, Editions du Centre national de la recherche scientifique, Paris, 1989, ISBN 9782222036869, p. 521.
29. Fernandes, C. P.; Magnani, F. S.; Philippi, P. C.; Daïan, J. F. Multiscale geometrical reconstruction of porous structures. Phys. Rev. E: Stat. Phys. Plasmas Fluids Relat. Interdiscip. Topics, 1996; 54: 1734-1741.
30. Fernandes, C. P. Caracterização Morfotopológica de Espaços Porosos: Reconstituição Multiescala e Simulação de Processos de Invasão de Fluidos Não-molhantes [Morphotopological characterization of porous spaces: Multiscale reconstitution and process simulation for the invasion of non-wetting fluids]. Doctoral thesis, Federal University of Santa Catarina, Florianópolis, Brazil, 1994.
31. Torquato, S.; Lu, B. Chord-length distribution for a two-phase random media. Physical Review E, 1993; 4: 2950–2953.
32. Damiani, M. C.; Fernandes, C. P.; Bueno, A. D.; Santos, L. E. O.; Cunha Neto, J. A. B.; Philippi, P. C. Predicting Physical Properties of Reservoir Rocks from the Microestrutural Analysis of Petrographic Thin Sections, Aplicaciones de la Ciencia en la Ingeniería de Petróleo, Foz de Iguaçu, May 08-12/2000.
33. Imago® User Manual, Ver. 2.4. 11, ESSS - Engineering Simulation and Scientific Software©, 88; 2002.
34. Truscello, S.; Kerckhofs, G.; Van Bael, S.; Pyka, G.; Schrooten, J.; Van Oosterwyck, H. Prediction of permeability of regular scaffolds for skeletal tissue engineering: a combined computational and experimental study. Acta Biomater. 2012; 8: 1648–1658.
35. Acosta Santamaría, V.; Deplaine, H.; Mariggió, D.; Villanueva-Molines, A. R.; García-Aznar, J. M.; Gómez Ribelles, J. L.; Doblaré, M.; Gallego Ferrer, G.; Ochoa, I. Influence of the macro and micro-porous structure on the mechanical behavior of poly(L-lactic acid) scaffolds. J. Non Cryst. Solids, 2012; 358: 3141–3149.
36. Dias, M. R.; Fernandes, P. R.; Guedes, J. M.; Hollister, S. J. Permeability analysis of scaffolds for bone tissue engineering. J. Biomech. 2012; 45: 938–944.
37. Ochoa, I.; Sanz-Herrera, J. A.; Garcia-Aznar, J. M.; Doblaré, M. Permeability evaluation of 45S5 bioglass-based scaffolds for bone tissue engineering. J. Biomech. 2009; 42: 257–260.
38. Innocentini, M. D. M.; Faleiros, R. K.; Pisani Jr, R.; Thijs, I.; Luyten, J.; Mullens, S. Permeability of

porous gelcast scaffolds for bone tissue engineering. Journal of Porous Materials, 2009; 17: 615–627.
39. Lee, K. W.; Wang, S.; Lu, L.; Jabbari, E.; Currier, B. L.; Yaszemski, M. J. Fabrication and characterization of poly(propylene fumarate) scaffolds with controlled pore structures using 3D printing and injection molding. Tissue Eng. 2006; 12: 2801–2811.
40. Li, S.; De Wijn, J. R.; Li, J.; Layrolle, P.; De Groot, K. Macroporous biphasic calcium phosphate scaffolds with high permeability/porosity ratio. Tissue Eng. 2003; 9: 535–548.
41. Sepulveda, P.; Ortega, F.; Innocentini, M. D. M.; Pandolfelli, V. C. Properties of highly porous hydroxyapatite obtained by the gelcasting of foams. J. Am. Ceram. Soc. 2001; 83: 3021–3024.
42. Lim, T. H.; Hong, J. H. Poroelastic properties of bovine vertebral trabecularbone. J. Orthop. Res. 2000; 18: 671–677.
43. Grimm, M. J.; Williams, J. L. Measurement of permeability in calcaneal trabecular bone. J. Biomech. 1997; 30: 743–745.
44. Beaudoin, A. J.; Mihalko, W. M.; Krause, W. R. Finite element modeling of polymethylmethacrylate flow through cancellous bone. J. Biomech. 1991; 24: 127–136.
45. Feldkamp, L. A.; Davis, L. C.; Kress, J. W. Practical cone-beam algorithm. J. Opt. Soc. Am. A, 1984; 1: 612-619.